Single-Cell Confinement on Micropatterned Glass Substrates: An AFM Analysis of Cell Height and Topography

Daniele Pedroni, Caroline Gaucher, Halima Alem

Single-Cell Confinement on Micropatterned Glass: an AFM Topographical Profiling

Journal:	*Langmuir*
Manuscript ID	la-2025-026097
Manuscript Type:	Article
Date Submitted by the Author:	22-May-2025
Complete List of Authors:	Pedroni, Daniele; Institut Jean Lamour, N2EV Gaucher, Caroline; Universite de Lorraine, CITHEFOR EA 3452 Alem, Halima; Universite de Lorraine, Institut Jean Lamour

Graphical Abstract

Single-Cell Confinement on Micropatterned Glass: an AFM Topographical Profiling

Daniele Pedroni[1,2*], *Caroline Gaucher*[2] *and Halima Alem*[1]

[1]Université de Lorraine, CNRS, IJL, F-54000 Nancy, France

[2]Université de Lorraine, CITHEFOR, F-54000 Nancy, France

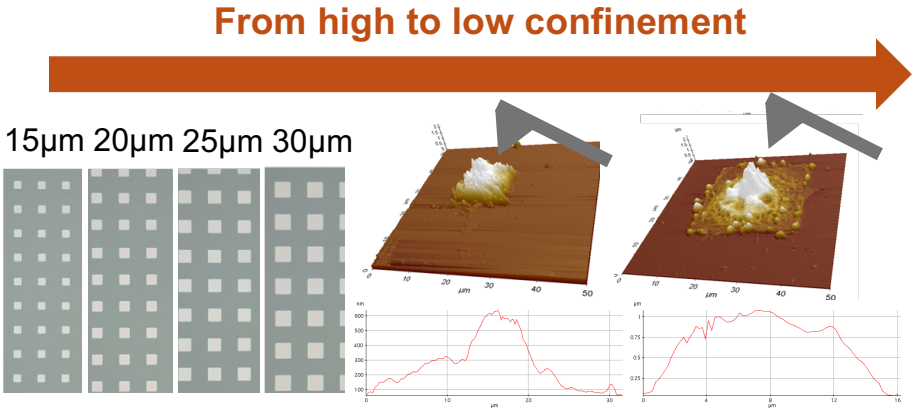

Confinement modulates cell height and surface roughness. Deep AFM analysis reveals morphological and nanomecchanical shifts

Single-Cell Confinement on Micropatterned Glass: an AFM Topographical Profiling

Daniele Pedroni[1,2], Caroline Gaucher[2] and Halima Alem[1]*

[1]Université de Lorraine, CNRS, IJL, F-54000 Nancy, France

[2]Université de Lorraine, CITHEFOR, F-54000 Nancy, France

Keywords: Micropatterning, Atomic Force Microscopy (AFM), Endothelial Cells, Cell Topography, Surface Roughness

Abstract

Atomic Force Microscopy (AFM) offers nanometrical resolution for analyzing cellular topography and mechanical properties. However, the inherent irregularity of cell morphology, the different stages of the cell cycle and the inter-cell interaction inside a culture often complicates accurate measurements. To overcome this limitation, we employed micropatterning techniques to standardize cell shape by forcing endothelial cells to adopt a uniform, square configuration. Cells were cultured on microfabricated substrates featuring

square patterns of 10, 15, 20, 25, and 30 μm side. Following silanization and cell seeding, individual cells conformed to these defined geometries, permitting consistent AFM scans through the entire area of cells. We extracted key topographical parameters, including the average and RMS height profiles, root mean square slope (Sdq), as well as higher-order statistics such as kurtosis and skewness. A high-pass filter was applied to isolate local surface roughness from overall cell shape. Our analysis revealed significant differences in both height and roughness parameters between cells confined to smaller *versus* larger patterns, indicating that the available adhesion area critically influences cell morphology. Notably, kurtosis and skewness metrics further underscored distinct differences in height distribution across the various pattern sizes. These findings demonstrate that combining micropatterning with AFM provides a robust platform for single-cell studies, offering enhanced reproducibility and deeper insights into how controlled cell shape modulates surface properties and cellular function.

Introduction

Characterizing single-cell topography and mechanics is crucial for understanding cellular function, but conventional methods struggle with cell-to-cell variability. Atomic Force Microscopy (AFM) is a powerful imaging technique that enables high-resolution topographical analysis of surfaces at the nanometer scale. Unlike optical and electron microscopy, AFM operates by scanning a sharp probe over the sample surface, measuring the interaction forces between the tip and the sample[1,2]. Its various operational modes and the modularity of key components, such as the tip shape, have paved the way for the use of AFM in numerous biomedical applications[3,4]. These include the study of the physical and mechanical properties of biological elements and biomaterials, such as cells and bacterial membrane [4–9], as well as

investigations into the nature of interactions between specific components, such as proteins or drugs[10,11]. Moreover, the data collected through AFM have been a useful integration when coupled with other forms of microscopy, such as confocal[12,13], fluorescence[14,15], Raman[16] and optical microscopy[17]. Traditional bulk analysis methods often overlook cell-to-cell variability, making the characterization of single cells an important step for obtaining precise and representative data[18]. Therefore, the study of single-cell properties may be the answer for understanding fundamental biological processes, disease mechanisms, and cell responses to external stimuli[19,20]. AFM has been widely employed for those studies due to its ability to provide mechanical characterization at the nanoscale[21–24]. The main difficulty remains in single-cell isolation and culture on a substrate. To that purpose, multiple techniques have been previously employed to isolate and analyze single cells such as microfluidics traps or fluorescence activated cell sorting[25]. Micropatterning, a type of treatment that allows localized surface modifications to be created to tune local bio-adhesive potential might be propose to isolate one cell from another. Micropatterning is usually achieved by "printing" protein patterns on a specific surface using an elastomeric mold, such as PDMS, and then passivating the remaining surface with bovine serum albumin[26,27], Pluronic f-127[28], or polyethyleneglycol-L-polylacticacid[29]. Another possibility is to take advantage of surface chemistry to covalently modify its adhesive properties, for example by using silane composites associated with a passivating agent like PEG[30–32]. After that, the patterning process can be achieved either by photopatterning [14,33,34] or through sacrificial structures to "mask" localized parts of the surface from chemical treatment[35,36].

The goal of this work is to isolate single human umbilical vein endothelial cells (HUVECs) through a micropatterning technique and to take advantage of the regular shape imposed by the patterning to perform a full single-cell study of its topographical and volumetric features and highlight the changes that occur within the same type of cells by varying the extension of the available surface. To achieve this goal, HUVECs will be cultured on of 15 μm, 20 μm, 25 μm, and 30 μm (length of a square side) glass patterns surrounded by passivated, non-adhesive surface. These measures have been chosen since, in previous works, single-cell patterning have been observed for measures around 30 μm width for different type of cells[33,34,37–41], while 15 μm square size was the smallest dimension where a regular square shape was maintained by the patterned cells. In summary, by confining single cells on micro-fabricated islands of defined size, we aim to analyze how the available adhesion area affects cell height and surface roughness (via AFM). We hypothesize that smaller adhesive areas will induce noticeable increases in cell height and changes in topographical distribution.

Materials and Method

Production of Micropatterned glass surfaces

The production of the micropatterned glass surface has been performed as in previous experiments (Pedroni et al.[42]).Briefly, a Borofloat glass wafer 2"300±20/DSP/Ra<1.2nm (Siegert Wafer, DE) was treated with oxygen plasma (Tucano plasm a system, Gambetti Vacuum Solution, IT) at 200 W for 300 s. After that, the surface was covered with a 5 nm aluminium layer using a Kenosistec KS400HR sputtering machine (Kenosistec, IT), then a

resist ARN 7500.18 (Allresist, DE) was spin-coated on the cleaned surface of the sample for 60 s at 5000 rpm and later heated for 60 s at 85˚C on a hotplate.

Electron-beam lithography was performed on the sample using a Raith 150 E-Beam-Writer (Raith, DE). Four different patterns were produced, consisting in matrices squares of 15 μm, 20 μm, 25 μm, and 30 μm side separated by 30 μm from one another. Each pattern contained only one type of square, and the different patterns were vertically separated by 5 mm of empty space. Once the process was concluded, the sample was developed with MF319 developer for 90 s.

The glass surface was treated with O_2 plasma (50W, 60s) to be activated prior to being inserted inside the glass reactor chamber to perform gas-phase deposition. Then, the chamber was put under partial vacuum (7 mbar) for 4 min and 0.4 ml of 2-[Methoxy(polyethyleneoxy)propyl]trimethoxysilane (abcr, DE) was aspirated inside the chamber through a valve-controlled opening. The sample was kept inside the reactor at 85˚C for 24 h. After that, it was removed from the chamber, and the excess silane and the resist were cleaned through 20 min of ultrasound in isopropanol. The remaining aluminum was removed with a further 90 s rinsing in MF319 developer. The micropatterned glass surface was finally cleaned with isopropanol and stored at room temperature until observation with reflected microscopy (Leica DM80000M) and/or cell seeding.

Cellularization of Micropatterned glass surfaces

Human umbilical vein endothelial cells (PromoCell GmbH, Heidelberg, DE) were cultured at 37 ˚C under 5% CO_2, using endothelial cell growth medium supplied with basal medium and supplement mix (Sigma-Aldrich, USA). This supplemented medium contains fetal calf serum (2% v/v), endothelial cell growth supplement (0.4% v/v), epidermal growth factor (recombinant

human) (0.1 ng/ml), basic fibroblast growth factor (recombinant human) (1 ng/ml), heparin (90 µg/ml), and hydrocortisone (1 µg/ml). All cells used were between passage four and eight, with media exchange every 48 hours.

Micropatterned glass surfaces were immersed for 30 min in a 70% ethanol solution in water, rinsed three times in fresh Dulbecco's phosphate buffered saline (PBS, Sigma-Aldrich, USA) and seeded with HUVECs at $10*10^3$ cells/cm² in supplemented medium. Cellularized samples were then placed at 37 ˚C in an incubator under 5% CO_2 for 6 before being were rinsed with PBS and fixed for 20 min with 4% m/v paraformaldehyde solution in PBS. Cellularized micropatterned glass surfaces were finally stored in PBS at 4˚C until analysis.

Morphological analysis of cells

Contrast phase observation

Cellularized micropatterned glass surfaces have been observed in phase contrast mode with a ZEISS AX10 inverted microscope equipped with and Axiocam 202 mono. The software employed for the imaging were the LAS software for the reflected microscopy and ZEN 3.1 for the inverted microscopy.

Topographic and volumetric analysis

Prior to the experiment, the sample was dried by sequential immersion in progressive ethanol solutions. Briefly, the PBS was removed, and the surface was immersed for 5 minutes in a 25% ethanol solution in distilled water, which was later removed and substituted with a solution of 50% ethanol in distilled water for 5 minutes. The procedure was repeated for a 75% ethanol/distilled water solution and 100% ethanol, after which the sample was put under partial vacuum (7mbar) for 30 minutes.

The dried sample was then placed inside the Park Systems NX10 (Park Systems, Kr) Atomic Force Microscope, and multiple single-cell scans were taken for each type of pattern using Non-Contact Mode (NCM) with an OMCL-AC160TS 10M Non-Contact Cantilever from the same supplier.

The scans were acquired on a 50μm side square surface containing a single patterned cell with a 256-square-pixel resolution and a resonance frequency between 242 and 247Hz, with a scan rate of 10-20Hz on the cells. The images were observed using XEI software (Park Systems, Kr) and flattened using a first-degree polynomial.

Statistical Analysis

Using the XEI software, the average profile of a patterned cell was acquired for each scan. A "profile" is the plot of every height measurement of a single linear scan, while the "average profile" is the plot of the mean of every measurement on the Y-axis, given a linear scan on the X-axis. The direction and length on X and Y are arbitrary, and the resulting area was set to be the closest square on the X-axis (scan length [μm]) to include any height measurements outside the pattern whenever present.

The resulting average profiles for n=10 scans for each class of pattern dimension were exported to Excel software, where the mean and standard error were calculated for each point on the X-axis.

Area under curve (AUC) was extracted from each profile by integration using the trapezoidal rule :

$$\sum_{i=1}^{n-1} \frac{f(x_i) + f(x_{i+1})}{2} \cdot (x_{i+1} - x_i)$$

As a mean to compare the different cell profiles, the AUC of each class of dimension have been compared trough Kruskal-Wallis ANOVA followed Dunn's test for pairwise comparisons (OriginPro software). The null hypothesis was rejected for $p<0.05$. A non-parametric test was chosen after demonstrating the non-normality of of the 25 μm size distribution through Shapiro-Wilk normality test.

Using the surface analysis function of the XEI software, it was possible to calculate root mean square height (Sq), arithmetic mean height (Sa), kurtosis (Sku), skewness (Ssk), maximum height of the peaks (Sk), and root mean square slope (Sdq).

To study the surface roughness, the scans were filtered through a high-pass filter (kernel = 3) to eliminate the "slow" changes in topography. This expedient allowed for the removal of the actual shape of the cell, leaving only the localized surface texture to be considered. This approach made it possible to analyze the root mean square roughness (RMS Roughness), the arithmetic average roughness, the root mean slope roughness, the core void volume, and the core material volume.

The Sq and the RMS Roughness are measured as follows:

$$S_q = \sqrt{\frac{1}{A} \iint_A z^2(x,y)\ dx\, dy}$$

The height is indicated with "z" and the flat surface area on which the measurement is conducted with "A". Sq and RMS roughness are useful to be compared to the (Sa) and

arithmetic mean roughness, since it gives an increased importance to high peaks and valley. This value is amplified by its square elevation, while the arithmetic parameters are measured as it follows:

$$S_a = \frac{1}{A}\iint_A |z(x,y)|\ dx\,dy$$

Kurtosis of topography height distribution, Sku, is a parametric measurement of the steepness of the height distribution of a surface[43]. By convention, a sku > 3 indicates a leptokurtotic behaviour of the height distribution, with a sharp peak indicating a high concentration of height measurement around a single parameter, while a sku < 3 indicates a platikurtotic behaviour, and therefore a more distributed number of the height measurements through the entire vertical projection of the structure.

$$S_{ku} = S_q^{-4}\left(\frac{1}{A}\iint_A z^4(x,y)\ dx\,dy\right)$$

The skewness (ssk) of the height distribution is a statistical parameter that describes the asymmetry of the surface height values relative to the base surface and gives an indication of how high the average height is compared to the total height span of the analyzed surface.

$$S_{sk} = S_q^{-3}\left(\frac{1}{A}\iint_A z^3(x,y)\ dx\,dy\right)$$

Sp is the maximum height of the peaks, which is the maximum height value registered on any given cell at any scan.

The Root Mean Square Slope (sdq) is a value used to assess regularity of a surface by measuring the average slope angle (expressed in radiant) on a given area, and is expressed as it follows:

$$S_{dq} = \sqrt{\frac{1}{A}\iint_A \left[\left(\frac{\partial z(x,y)}{\partial x}\right)^2 + \left(\frac{\partial z(x,y)}{\partial y}\right)^2\right] dx\ dy}$$

Where A is the given flat surface area, z(x,y) the function of the surface while $(\frac{\partial z(x,y)}{\partial x})^2$ and $(\frac{\partial z(x,y)}{\partial y})^2$ are the partial derivatives of the function z(x,y) on both axis. Core void volume (VVC') and core material volume (VMC') are both volume-based measurements that rely on the concept of the Abbot-Firestone curve, which shows the percentage distribution of the volume relative to the height of the surface measurement. Conventionally, the term "core" refers to the portion of the curve between 10% and 80%, thus excluding the deepest pits and the highest peaks relative to the actual volume measured.

VVC' and VMC' represent, respectively, the void and the material volume within the core area of the roughness of each cell. Both parameters are calculated on the filtered scans.

All these parameters were measured on the cell surface, taking advantage of the square shape imposed by the chemical patterning to avoid including external, unrelated measurements in the computation.

For each size class, n= 10 cells for each class of dimension were scanned, resulting in the same number of average profile assessments and measurements for each of the listed roughness parameters. The experimental conditions allowed individual cells to be scanned and enabled analysis of the full surface of each cell.

Resulting data were compared using Kruskal-Wallis ANOVA followed Dunn's test for pairwise comparisons (OriginPro software). The null hypothesis was rejected for $p<0.05$.

Results and Discussion

After lithography, the resulting micrometrical structures have been observed by contrast phase microscopy (Figure 1). E-beam lithography is a well-known technique for producing micro and nanometrical features on various types of conductive surfaces and has a long history of application in the molecular patterning either by local modification of the surface parameters or through sacrificial structures [35,44–46] . While the use of this machine is commonly indicated for conductive surfaces such as silicon, it can be employed on insulating surfaces, such as glass, as long as they are covered with a layer of conductive material like aluminum, chromium or copper [47,48]. Figure 1 observations validate the microfabrication process with squares of desired dimension and spacing.

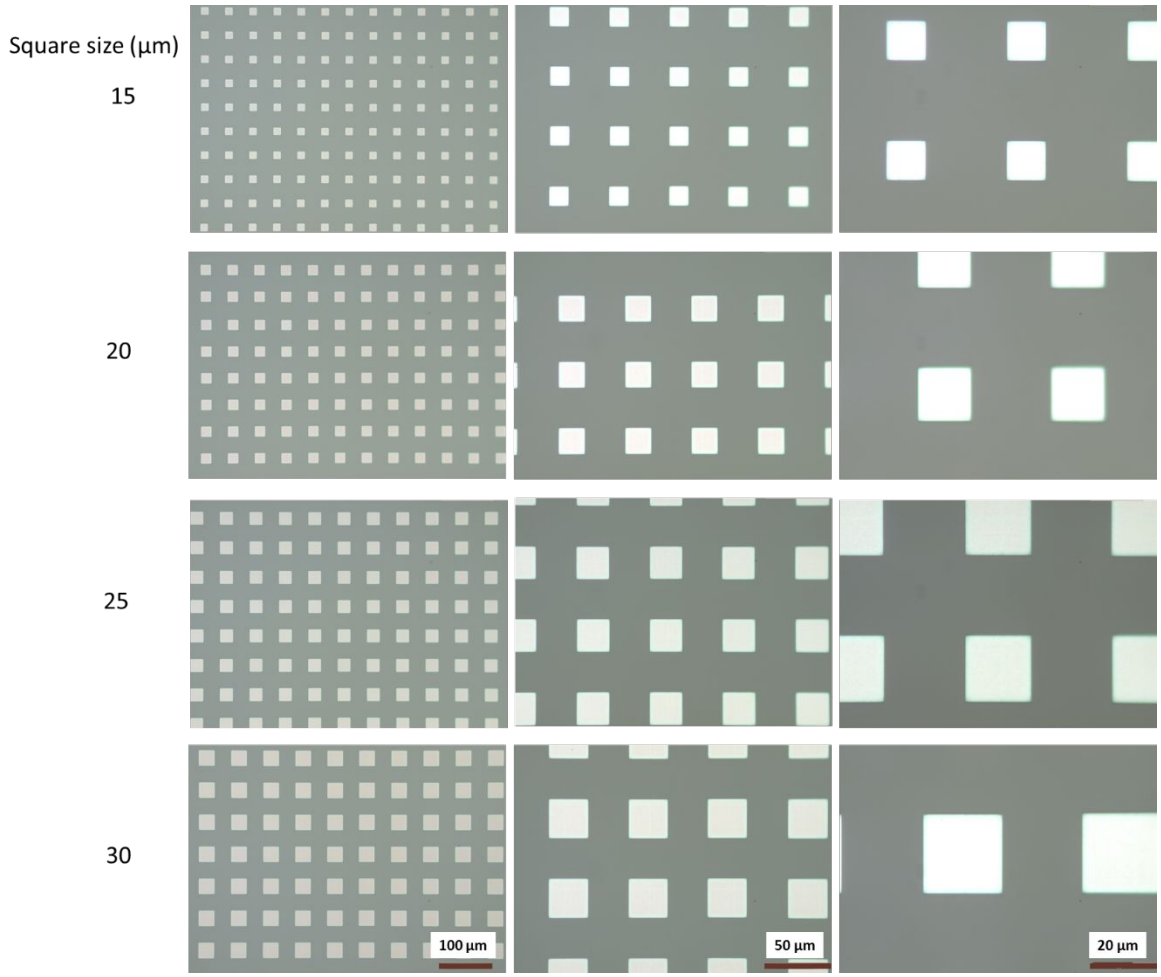

Figure 1. Representative images of glass resist structures with different square sizes spaced by 30 µm. Images acquired with a reflected light microscope (Leica DM80000M).

Six hours after seeding on silanized glass surface, cells display the same shape and spacing as the sacrificial structures for all classes of dimension (Figure 2). Our observation confirmed the results obtained by other studies, that reached the same results with patterns of comparable sizes and shapes and with different types of cells[33,34,37–41], while the presence of multiple cells has been noted on square patterns of 60 µm size[49]. Moreover, it was also shown that other shapes such as linear or rectangular pattern larger than 30 µm would occasionally host more than one cell at a time[50], while this does not seem to occur with squares of 30 µm size as we observed.

Indeed, in our experiment, each cellularized square seemed to host only one cell, and none of the microscope observation or AFM scan indicate otherwise. Finally, the square spacing of 30 µm, chosen to minimize interactions between cells located on different squares, as observed by others in between 20 µm[38] and 30 µm[51], is enough to maintain cell isolation after 6 h.

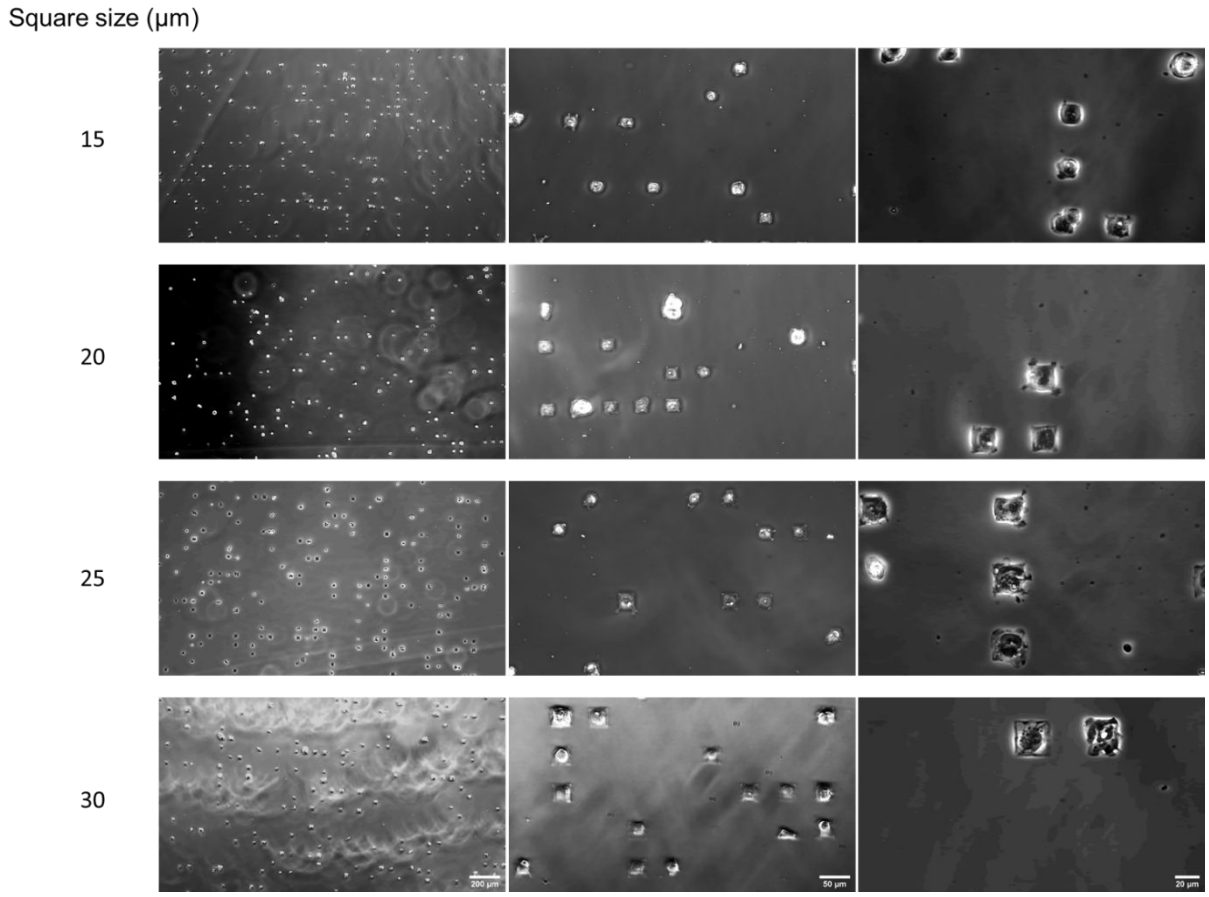

Figure 2. Representative images of HUVECs on micropatterned glass surfaces 6 h after seeding on different square sizes spaced by 30 µm. Images acquired with a phase contrast microscope (ZEISS AX10 equipped with and Axiocam 202 mono)

After six hours, cells were fixed in paraformaldehyde, and the surface was dehydrated through immersion into progressive ethanol. Both procedures are known to preserve cell shape

and topography[52–54 55]. Then, cells were individually scanned by AFM. Each scan included an area of a 50%μm × 50%μm area and a single patterned cell regardless of its dimension. Consistently with phase-contrast microscope observations (Figure 2), all scanned cells assume the shape of one of the 4 square patterns present on the micropatterned glass surface (**Error! Reference source not found.** a, b, c, d). For each scan, the average profile was extracted through the entire length of each scanned cell. The "profile" is the graphical representation of the heights of a structure scanned along a line, while the "average profile" is the graph resulting from the mean of every height measurement on the same Y-axis.

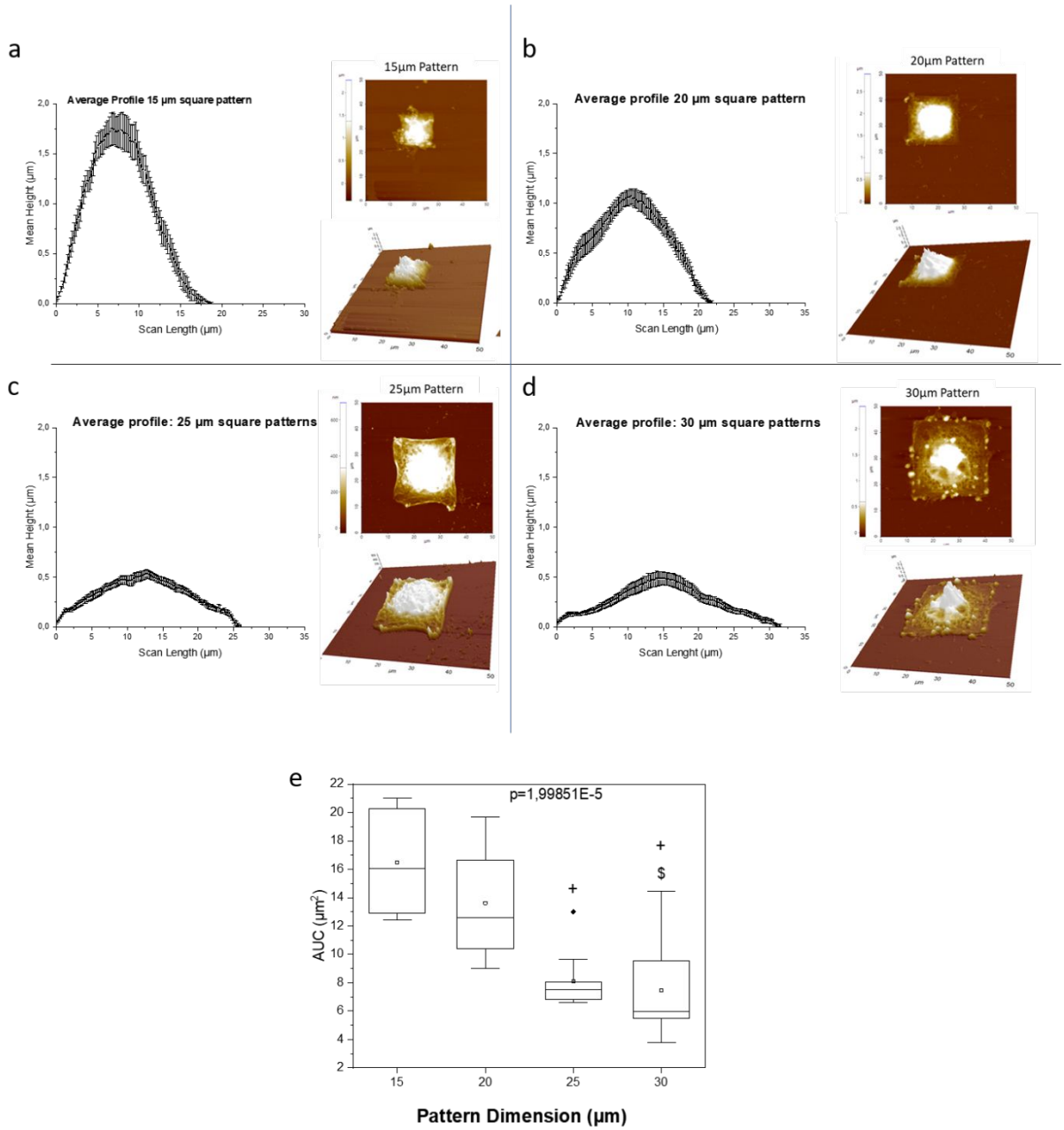

Figure 3. Average height profile of HUVECs and 2d and 3d topography maps of HUVECs fixed patterned glass. Acquisition made with Park Systems AX10. Images where flattened with XEI software (Park Systems, Kr) ; (a) 15µm square, (b) 20µm square; (c) 25µm square; (d) 30 µm square

The height profile of different cells has been measured in previous works and is usually represented as either the cross-section, the maximum height, or the average of multiple profiles

sampled from different cells[16,24,56–59]. The reason why the single scan line is used as the main representation of the cell profile is likely due to the irregular and rather unpredictable shape of the cells in static conditions, which would result in parameters like the average profile being used exclusively for limited sections of the cell. Performing a scan on a square (or rectangular) patterned cell would guarantee the possibility to observe the average profile of the entire cell through its total surface while minimizing the risk of background noise in the data.

Error! Reference source not found. (a, b, c, d) presents the resulting average profile of 10 cells scanning per pattern dimension to decipher which areas of the cell show the highest variation. There is an evident difference between the shapes of the profiles both along the X-axis (the scan length) and the height of the different curves. As observed on the 15 µm and 20 µm, the reduction of the available surface for colonization brings the cells to adopt higher profile and overall, a higher average height compared to cells distributed on larger 25 µm and 30 µm areas. Specifically, while there is an evident difference in average height of cells seeded on 10 µm, 20 µm, and 25 µm or 30 µm side squares, there is no difference between 25 µm and 30µm. The measurement of the AUC trough the integration of the curves allows for a comparison between the different dimension, as it can considered the average section area for the patterned cells. In Figure 3e, statistical analysis confirms an overall difference between 15 µm square patterned cells and the 25 µm and 30 µm classes, suggesting that a limitation of the adhesive surface might cause an higher average area of the section and therefore an higher volume concentration per unit of length compared to cells with larger surface to colonize. As confirmed by the qualitative observations, there seems to be no difference in the average surface area between cells patterned on 25 µm and 30 µm square. In this specific case, while there is a

difference in the length of the cells along the scan axis due to the different dimensions of the pattern, there is little difference between the curves.

Full height parameters such as RMS, arithmetic mean average and maximum height (Figure 4 a, b and c) are consistent in showing a significant difference in the vertical measurements of cells on 10 μm or 15 μm compared to those cultured in 25 and 30 μm squares suggesting that a 10 μm change in a pattern dimension is enough to generate a significant difference in height. The highest peak is an important parameter for assessing how cell height changes depending on the amount of available surface, it must be noted that this kind of absolute measurement is the most prone to machine glitches or sample contamination. Despite these premises, Figure 4 c shows that maximum height changes significantly in the range of 20 to 25 μm in dimension, while measurements over a similar gap (25-30 μm and 15-20 μm) showed no significant difference.

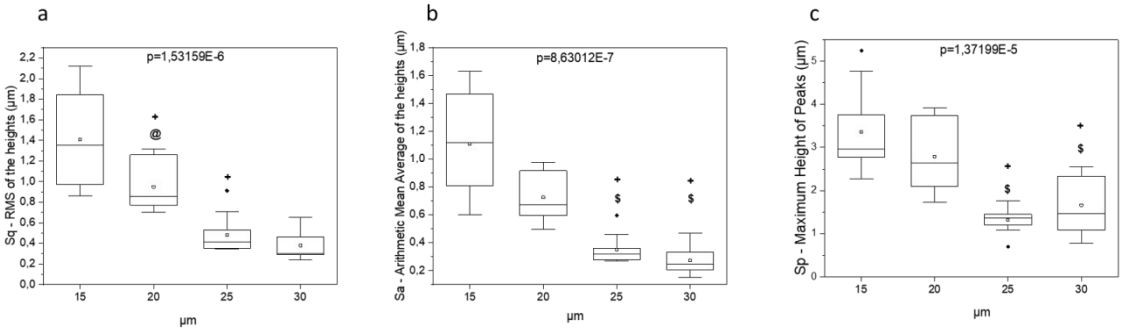

Figure 4. Surface analysis of HUVEC (a) Root mean square of the heights; (b) Arithmetic mean average of the heights; (c) Maximum height of the peaks. Statistical analysis and graphs are made with Kruskall-Wallis ANOVA followed by Dunn's test for multiple comparisons

(OriginPro) with $^{+}p < 0.05$ versus 15 μm and $^{\$}p < 0.05$ versus 20 μm and $^{@}p < 0.05$ versus 30 μm.

Then deeper in height investigation, the kurtosis value of height distribution (Figure 5a) indicates that cells patterned on 30 μm showed a significantly higher value compared to those patterned at 15 μm and 25 μm, while no difference with the distribution of cells patterned on 20 μm was observed. More specifically, while height distributions of cells patterned on 15 μm and 25 μm were slightly platykurtic (Sku < 3) with a flatter height distribution, the 30 μm patterned cells exhibited kurtosis values mostly concentrated around leptokurtic (Sku > 3) levels, signifying that the height measurements were more concentrated around similar values. This measurement becomes useful when applied over the full extent of cell, as it provides a rough indication of the distribution of cell volume over a known surface. When compared with other topographical parameters, it enables the assessment of various hypotheses regarding the height distribution among different subjects. For example, while the kurtosis values of the 20 μm and 30 μm patterned cells were not significantly different, both RMS height and average height comparisons between the same patterns rejected the null hypothesis, suggesting a significantly different height between cells patterned on 20 μm and those on 30 μm. These two parameters suggest that while cells patterned on a larger surface tend to have a concentration of values in the lower heights (a flatter base with sharp and steep peaks), cells patterned on smaller dimensions exhibit a rapid increase in height, leading to a flatter top. However, this assumption does not hold for the intermediate pattern dimensions of 15 μm and 25 μm. To validate the previous observations about the difference in steepness for the height distribution among the different classes of dimension, the RMS slope for the entire cells have been considered (Figure

5c). This measurement considers the variation in angle between subsequent measurement, and results in the rejection of the null hypothesis when comparing 15 μm patterned cells with the 25 μm and 30 μm patterns. These results are also consistent with height-related measurements in Figure 6. Surface analysis of HUVEC (a) Root mean square roughness; (b) Arithmetic mean roughness; (c) Root mean slope roughness; (d)VMC – Core material roughness; (e) VVC' Void Core Volume Roughness. Statistical analysis and graphs are made with Kruskall-Wallis ANOVA followed by Dunn's test for multiple comparisons (OriginPro) with $^{+}p < 0.05$ versus 15 μm and $^{\$}p < 0.05$ versus 20 μm and $^{@}p < 0.05$ versus 30 μm. 4 (a, b) and show a correlation between both the overall shape slope and cell height.

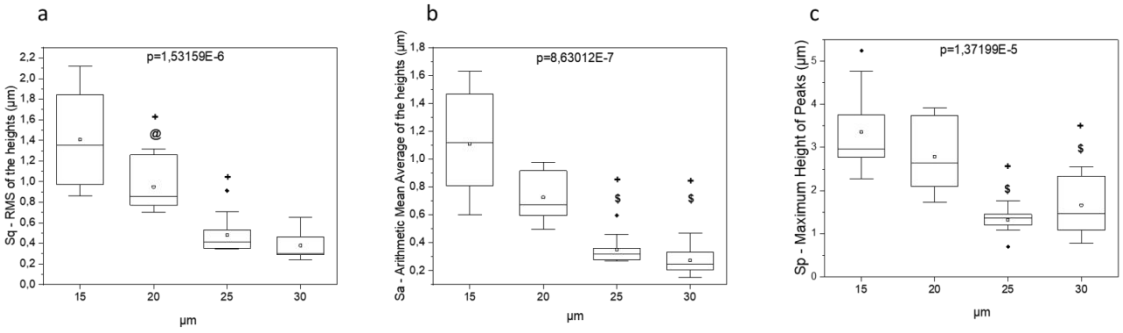

Figure 5. Surface analysis of HUVEC (a) Kurtosis of the height distribution; (b) Skewness of the height distribution; (c)Root mean square slope for the full cell. Statistical analysis and graphs are made with Kruskall-Wallis ANOVA followed by Dunn's test for multiple comparisons (OriginPro) with $^{+}p < 0.05$ versus 15 μm and $^{\$}p < 0.05$ versus 20 μm and $^{@}p < 0.05$ versus 30 μm.

To evaluate cell surface roughness, a high-pass filter was used to remove the "slow" variations in height associated with the actual shape of cells, allowing isolation of only the "fast" high-frequency variations associated with surface roughness.

In the literature, previous observations on cell roughness were made through sampling different parts of the cells[60–63], due to experimental necessity, limitations of the equipment or the lack of a regular cell shape, but nonetheless, the results showed that cell roughness could be used as an indicator of cell status, such as oxidative stress [60] and the mechanical properties of the membrane[61] or the substrate[63].

Figure 6 (a, b) shows the average and RMS roughness for each class of dimension, highlighting that in both cases, the only significant difference was found between 15 μm patterns and the 25-30 μm ones, while the 20 μm patterned cells showed no difference with any of the other groups.

In **Error! Reference source not found.** (d, e) displays all the core-related values, with "core" indicating the portion of the cell surface within the range between 10%-80% of the total measured height (from the lowest valley to the highest peak). This definition derives from the concept of the Abbott-Firestone curve, or Material Ratio Curve (MRC), which represents the cumulative fraction of the surface area below a certain relative height. It is calculated through the integration of the distribution of measured surface heights and provides important insights into the sample topography. The parameters considered were the Core Material Volume (VMC') and Core Void Volume (VVC') the of cells in relation to their surface roughness. As observed, while the data distribution for cells patterned pattern between 15 μm and 25 μm squares showed no significant differences between one another, the 30 μm patterned cells

surfaces exhibited both a higher surface core volume and a higher VVC' compared to all the other categories. This result aligns with the kurtosis values (**Error! Reference source not found.** b), which revealed a higher concentration of values (expressed as Sku >> 3) compared to most of the other categories, a significantly lower height (Figure 4 a, b) and slope (Figure 5 c), and a visibly lower profile compared to the 10µm and 20µm patterns (**Error! Reference source not found.** a, b). The roughness parameters were consistent with all other categories except for 15 µm.

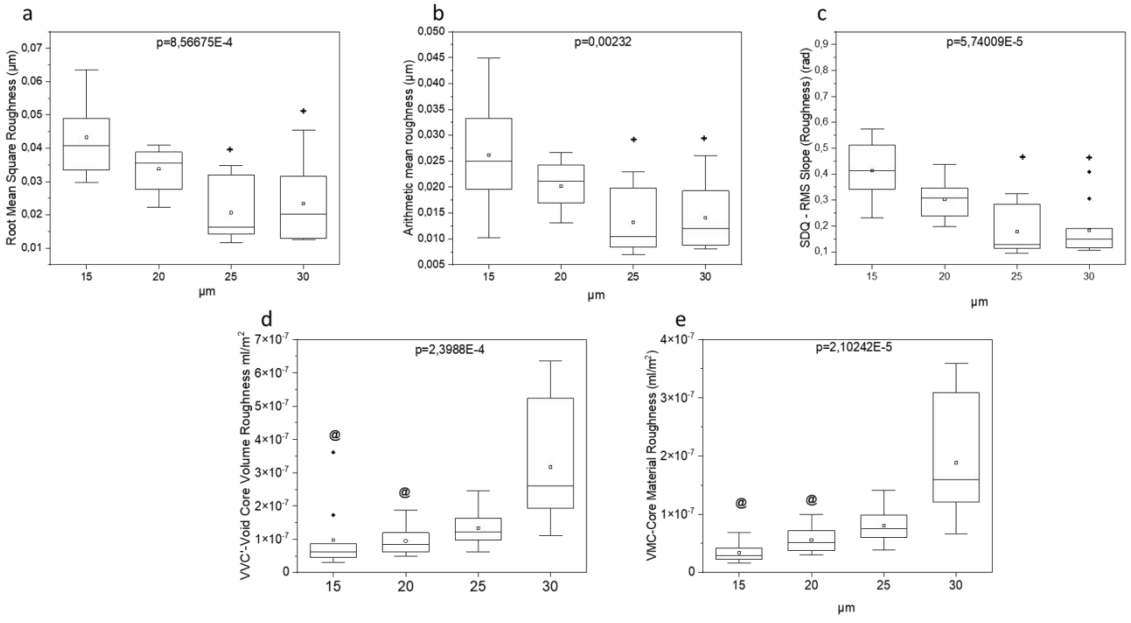

Figure 6. Surface analysis of HUVEC (a) Root mean square roughness; (b) Arithmetic mean roughness; (c) Root mean slope roughness; (d)VMC – Core material roughness; (e) VVC' Void Core Volume Roughness. Statistical analysis and graphs are made with Kruskall-Wallis ANOVA followed by Dunn's test for multiple comparisons (OriginPro) with $^{+}p < 0.05$ versus 15 µm and $^{\$}p < 0.05$ versus 20 µm and $^{@}p < 0.05$ versus 30 µm.

These data suggest that the 30 μm patterned cells exhibit a flatter surface with a slow increase in height, an overall lower profile, and a surface roughness comparable to most other distributions but less steep, as suggested by the Sdq measurements (**Error! Reference source not found.** c and Figure 6 c). The 25 μm surfaces share similar characteristics in height, roughness, and slope but significantly differ in terms of height distribution and surface volume distribution (Figure 5 a and b; Figure 6 d). These results suggest that the 30 μm patterned cells, while mostly flat, contains some small and steep elements that simultaneously produce a height distribution with a longer right tail with high skewness (**Error! Reference source not found.** a) and highly leptokurtotic profile (**Error! Reference source not found.** b).

Conclusion

This study posed itself the goal to enhance the reproducibility and accuracy of AFM measurements of single-cell topography trough micropatterning, by imposing a regular, square geometry on the substrate. Our results indicate that endothelial cells cultured on micropatterned surfaces adopt a morphology that facilitates the extraction of key topographical parameters such as average and RMS height, slope (Sdq), maximum peak height, as well as statistical descriptors like skewness and kurtosis. Notably, we observed that a reduction in available surface area induces a significant increase in both the average and RMS height, with a clear differentiation between cells patterned 15 μm square surfaces compared to those cultured on bigger patterns (25–30 μm square). Moreover, cells on the largest pattern (e.g., 30 μm) exhibited a markedly higher kurtosis and skewness, suggesting a more concentrated height distribution with a pronounced right tail, likely reflecting the presence of sharp, steep features against a generally flat base. The integration of high-pass filtering further enabled us to isolate the high-frequency

components of surface roughness, allowing for a full cell measurement of membrane rugosity and texture. Collectively, these findings not only validate the use of micropatterning as a means to standardize cell shape and improve measurement precision but also underscore its potential to uncover subtle variations in cell mechanics and morphology that may have important biological implications. Future studies should focus on further investigating how additional factors might impact topographical characteristics, including the micropatterning technique used, the type of substrate and its mechanical properties, or the methods employed for sample fixation and drying prior to experimentation.

AUTHOR INFORMATION

Corresponding Authors

Daniele PEDRONI : daniele. pedroni@univ-lorraine.fr

Halima ALEM : halima.alem@univ-lorraine.fr

Author Contributions

The manuscript was written through contributions of all authors. All authors have given approval to the final version of the manuscript.

Acknowledgments

The work was supported by the French PIA project “Lorraine Université d’Excellence” reference ANR-15-IDEX-04-LUE. We are Thankfull to the CC Minalor platformfor their help and their advices.

ABBREVIATIONS

HUVECs Human umbilical vein endothelial cells; AFM Atomic Force Microscopy; PEG polyethylene glycol; PBS phosphate buffered saline; NCM Non-Contact Mode; AUC Area Under Curve; RMS Root mean Square; Sq RMS height; Sa arithmetic mean height; Sku kurtosis; Ssk skewness; Sk maximum height of the peaks; Sdq root mean square slope; VVC' Void core volume; VMC' core material volume

References

1. Binnig, G., Quate, C. F. & Gerber, C. Atomic Force Microscope. in *Scanning Tunneling Microscopy* (ed. Neddermeyer, H.) vol. 6 55–58 (Springer Netherlands, Dordrecht, 1993).

2. Buscarino, G. Atomic Force Microscopy and Spectroscopy. in *Spectroscopy for Materials Characterization* (ed. Agnello, S.) 425–460 (Wiley, 2021). doi:10.1002/9781119698029.ch15.

3. Vahabi, S., Nazemi Salman, B. & Javanmard, A. Atomic force microscopy application in biological research: a review study. *Iran J Med Sci* **38**, 76–83 (2013).

4. Kontomaris, S. V. & Stylianou, A. Atomic force microscopy for university students: applications in biomaterials. *Eur. J. Phys.* **38**, 033003 (2017).

5. Firtel, M., Henderson, G. & Sokolov, I. Nanosurgery: observation of peptidoglycan strands in Lactobacillus helveticus cell walls. *Ultramicroscopy* **101**, 105–109 (2004).

6. Muller, D. J. AFM: A Nanotool in Membrane Biology. *Biochemistry* **47**, 7986–7998 (2008).

7. Li, M., Dang, D., Liu, L., Xi, N. & Wang, Y. Atomic Force Microscopy in Characterizing Cell Mechanics for Biomedical Applications: A Review. *IEEE Trans.on Nanobioscience* **16**, 523–540 (2017).

8. Rianna, C. & Radmacher, M. Cell mechanics as a marker for diseases: Biomedical applications of AFM. in 020057 (Tomsk, Russia, 2016). doi:10.1063/1.4960276.

9. Kasas, S., Longo, G. & Dietler, G. Mechanical properties of biological specimens explored by atomic force microscopy. *J. Phys. D: Appl. Phys.* **46**, 133001 (2013).

10. Mingeot-Leclercq, M.-P., Deleu, M., Brasseur, R. & Dufrêne, Y. F. Atomic force microscopy of supported lipid bilayers. *Nat Protoc* **3**, 1654–1659 (2008).

11. Li, G., Xi, N. & Wang, D. H. Probing membrane proteins using atomic force microscopy. *J Cell Biochem* **97**, 1191–1197 (2006).

12. Haupt, B. J., Pelling, A. E. & Horton, M. A. Integrated Confocal and Scanning Probe Microscopy for Biomedical Research. *The Scientific World JOURNAL* **6**, 1609–1618 (2006).

13. Lehenkari, P. P. & Horton, M. A. Single Integrin Molecule Adhesion Forces in Intact Cells Measured by Atomic Force Microscopy. *Biochemical and Biophysical Research Communications* **259**, 645–650 (1999).

14. Shroff, S. G., Saner, D. R. & Lal, R. Dynamic micromechanical properties of cultured rat atrial myocytes measured by atomic force microscopy. *American Journal of Physiology-Cell Physiology* **269**, C286–C292 (1995).

15. Haga, H. *et al.* Elasticity mapping of living fibroblasts by AFM and immunofluorescence observation of the cytoskeleton. *Ultramicroscopy* **82**, 253–258 (2000).

16. Boitor, R., Sinjab, F., Strohbuecker, S., Sottile, V. & Notingher, I. Towards quantitative molecular mapping of cells by Raman microscopy: using AFM for decoupling molecular concentration and cell topography. *Faraday Discuss.* **187**, 199–212 (2016).

17. Cascione, M., De Matteis, V., Rinaldi, R. & Leporatti, S. Atomic force microscopy combined with optical microscopy for cells investigation. *Microscopy Res & Technique* **80**, 109–123 (2017).

18. Ding, L., Wendl, M. C., McMichael, J. F. & Raphael, B. J. Expanding the computational toolbox for mining cancer genomes. *Nat Rev Genet* **15**, 556–570 (2014).

19. Blainey, P. C. & Quake, S. R. Dissecting genomic diversity, one cell at a time. *Nat Methods* **11**, 19–21 (2014).

20. Van Loo, P. & Voet, T. Single cell analysis of cancer genomes. *Current Opinion in Genetics & Development* **24**, 82–91 (2014).

21. Lulevich, V., Zink, T., Chen, H.-Y., Liu, F.-T. & Liu, G. Cell Mechanics Using Atomic Force Microscopy-Based Single-Cell Compression. *Langmuir* **22**, 8151–8155 (2006).

22. Lekka, M. & Pabijan, J. Measuring Elastic Properties of Single Cancer Cells by AFM. in *Atomic Force Microscopy* (eds. Santos, N. C. & Carvalho, F. A.) vol. 1886 315–324 (Springer New York, New York, NY, 2019).

23. Hohmann, T. & Dehghani, F. Measuring Mechanical and Adhesive Properties of Single Cells Using an Atomic Force Microscope. in *Metastasis* (ed. Stein, U. S.) vol. 2294 81–92 (Springer US, New York, NY, 2021).

24. Zhou, X. *et al.* Reversed cell imprinting, AFM imaging and adhesion analyses of cells on patterned surfaces. *Lab Chip* **10**, 1182 (2010).

25. Gross, A. *et al.* Technologies for Single-Cell Isolation. *IJMS* **16**, 16897–16919 (2015).

26. Karimian, T., Hager, R., Karner, A., Weghuber, J. & Lanzerstorfer, P. A Simplified and Robust Activation Procedure of Glass Surfaces for Printing Proteins and Subcellular Micropatterning Experiments. *Biosensors* **12**, 140 (2022).

27. Nishizawa, M., Takoh, K. & Matsue, T. Micropatterning of HeLa Cells on Glass Substrates and Evaluation of Respiratory Activity Using Microelectrodes. *Langmuir* **18**, 3645–3649 (2002).

28. Bautista, M., Fernandez, A. & Pinaud, F. A Micropatterning Strategy to Study Nuclear Mechanotransduction in Cells. *Micromachines* **10**, 810 (2019).

29. Gao, D., Kumar, G., Co, C. & Ho, C.-C. Formation of Capillary Tube-like Structures on Micropatterned Biomaterials. in *Oxygen Transport to Tissue XXIX* (eds. Kang, K. A., Harrison, D. K. & Bruley, D. F.) vol. 614 199–205 (Springer US, Boston, MA, 2008).

30. Badv, M., Imani, S. M., Weitz, J. I. & Didar, T. F. Lubricant-Infused Surfaces with Built-In Functional Biomolecules Exhibit Simultaneous Repellency and Tunable Cell Adhesion. *ACS Nano* **12**, 10890–10902 (2018).

31. Noiri, M. *et al.* Influence of cell adhesive molecules attached onto PEG-lipid-modified fluid surfaces on cell adhesion. *Colloids and Surfaces B: Biointerfaces* **175**, 375–383 (2019).

32. Saneinejad, S. & Shoichet, M. S. Patterned glass surfaces direct cell adhesion and process outgrowth of primary neurons of the central nervous system. *J. Biomed. Mater. Res.* **42**, 13–19 (1998).

33. Azioune, A., Storch, M., Bornens, M., Théry, M. & Piel, M. Simple and rapid process for single cell micro-patterning. *Lab Chip* **9**, 1640 (2009).

34. Fink, J. *et al.* Comparative study and improvement of current cell micro-patterning techniques. *Lab Chip* **7**, 672–680 (2007).

35. Pallandre, A., Glinel, K., Jonas, A. M. & Nysten, B. Binary Nanopatterned Surfaces Prepared from Silane Monolayers. *Nano Lett.* **4**, 365–371 (2004).

36. Kim, D. J., Lee, J. M., Park, J. & Chung, B. G. A self-assembled monolayer-based micropatterned array for controlling cell adhesion and protein adsorption. *Biotech & Bioengineering* **108**, 1194–1202 (2011).

37. Dirscherl, C. & Springer, S. Protein micropatterns printed on glass: Novel tools for protein-ligand binding assays in live cells. *Engineering in Life Sciences* **18**, 124–131 (2018).

38. Chen, C. S., Mrksich, M., Huang, S., Whitesides, G. M. & Ingber, D. E. Micropatterned Surfaces for Control of Cell Shape, Position, and Function. *Biotechnol. Prog.* **14**, 356–363 (1998).

39. Chen, C. S., Mrksich, M., Huang, S., Whitesides, G. M. & Ingber, D. E. Geometric Control of Cell Life and Death. *Science* **276**, 1425–1428 (1997).

40. Sato, M., Levesque, M. J. & Nerem, R. M. Micropipette aspiration of cultured bovine aortic endothelial cells exposed to shear stress. *Arteriosclerosis* **7**, 276–286 (1987).

41. Gray, D. S. *et al.* Engineering amount of cell-cell contact demonstrates biphasic proliferative regulation through RhoA and the actin cytoskeleton. *Exp Cell Res* **314**, 2846–2854 (2008).

42. Pedroni, D., Gaucher, C., Ba, D., Badie, L., Raeth-Fries, I. & Halima, A. *Advanced Engineering Materials - under review*

43. *Machining and Tribology*. (Elsevier, 2022). doi:10.1016/C2019-0-00230-0.

44. Kolodziej, C. M. & Maynard, H. D. Electron-Beam Lithography for Patterning Biomolecules at the Micron and Nanometer Scale. *Chem. Mater.* **24**, 774–780 (2012).

45. McMurray, R., J, M. & Gadegaar, N. Nanopatterned Surfaces for Biomedical Applications. in *Biomedical Engineering, Trends in Materials Science* (ed. Laskovski, A.) (InTech, 2011). doi:10.5772/13453.

46. Kolodziej, C. M. *et al.* Combination of Integrin-Binding Peptide and Growth Factor Promotes Cell Adhesion on Electron-Beam-Fabricated Patterns. *J. Am. Chem. Soc.* **134**, 247–255 (2012).

47. Ermis, M., Antmen, E. & Hasirci, V. Micro and Nanofabrication methods to control cell-substrate interactions and cell behavior: A review from the tissue engineering perspective. *Bioact Mater* **3**, 355–369 (2018).

48. Samantaray, C. B. & Hastings, J. T. The effect of thin metal overlayers on the electron beam exposure of polymethyl methacrylate. *Journal of Vacuum Science & Technology B: Microelectronics and Nanometer Structures Processing, Measurement, and Phenomena* **26**, 2300–2305 (2008).

49. Segerer, F. J. *et al.* Versatile method to generate multiple types of micropatterns. *Biointerphases* **11**, 011005 (2016).

50. Wu, C.-C. *et al.* Directional shear flow and Rho activation prevent the endothelial cell apoptosis induced by micropatterned anisotropic geometry. *Proc. Natl. Acad. Sci. U.S.A.* **104**, 1254–1259 (2007).

51. Kam, L. & Boxer, S. G. Cell adhesion to protein-micropatterned-supported lipid bilayer membranes. *J Biomed Mater Res* **55**, 487–495 (2001).

52. Pollice, A. A. *et al.* Sequential paraformaldehyde and methanol fixation for simultaneous flow cytometric analysis of DNA, cell surface proteins, and intracellular proteins. *Cytometry* **13**, 432–444 (1992).

53. Mufson, E. J., Perez, S. E., Kelley, C. M., Alldred, M. J. & Ginsberg, S. D. Fixation Protocols for Neurohistology: Neurons to Genes. in *Neurohistology and Imaging Techniques* (eds. Pelc, R., Walz, W. & Doucette, J. R.) vol. 153 49–71 (Springer US, New York, NY, 2020).

54. Smit, J. W., Meijer, C. J. L. M., Decary, F. & Feltkamp-vroom, T. M. Paraformaldehyde fixation in immunofluorescence and immunoelectron microscopy. *Journal of Immunological Methods* **6**, 93–98 (1974).

55. Osorio, E., Toledano, M., Aguilera, F. S., Tay, F. R. & Osorio, R. Ethanol Wet-bonding Technique Sensitivity Assessed by AFM. *J Dent Res* **89**, 1264–1269 (2010).

56. Weber, A., Iturri, J., Benitez, R., Zemljic-Jokhadar, S. & Toca-Herrera, J. L. Microtubule disruption changes endothelial cell mechanics and adhesion. *Sci Rep* **9**, 14903 (2019).

57. Wu, Y. *et al.* The analysis of morphological distortion during AFM study of cells. *Scanning* **30**, 426–432 (2008).

58. Hecht, E. *et al.* Combined Atomic Force Microscopy–Fluorescence Microscopy: Analyzing Exocytosis in Alveolar Type II Cells. *Anal. Chem.* **84**, 5716–5722 (2012).

59. Docheva, D. *et al.* Researching into the cellular shape, volume and elasticity of mesenchymal stem cells, osteoblasts and osteosarcoma cells by atomic force microscopy. *J Cellular Molecular Medi* **12**, 537–552 (2008).

60. Wang, D.-C., Chen, K.-Y., Tsai, C.-H., Chen, G.-Y. & Chen, C.-H. AFM membrane roughness as a probe to identify oxidative stress-induced cellular apoptosis. *Journal of Biomechanics* **44**, 2790–2794 (2011).

61. Lee, C.-W. *et al.* Membrane roughness as a sensitive parameter reflecting the status of neuronal cells in response to chemical and nanoparticle treatments. *J Nanobiotechnol* **14**, 9 (2016).

62. D Antonio, P., Lasalvia, M., Perna, G. & Capozzi, V. Scale-independent roughness value of cell membranes studied by means of AFM technique. *Biochimica et Biophysica Acta (BBA) - Biomembranes* **1818**, 3141–3148 (2012).

63. Chang, C.-H., Lee, H.-H. & Lee, C.-H. Substrate properties modulate cell membrane roughness by way of actin filaments. *Sci Rep* **7**, 9068 (2017).